

Pixel-by-pixel deconvolution of bolus-tracking data: optimization and implementation

This content has been downloaded from IOPscience. Please scroll down to see the full text.

2007 Phys. Med. Biol. 52 429

(<http://iopscience.iop.org/0031-9155/52/2/009>)

View [the table of contents for this issue](#), or go to the [journal homepage](#) for more

Download details:

IP Address: 128.6.218.72

This content was downloaded on 09/09/2015 at 15:07

Please note that [terms and conditions apply](#).

Pixel-by-pixel deconvolution of bolus-tracking data: optimization and implementation

S Sourbron^{1,2}, M Dujardin², S Makkat² and R Luypaert²

¹ Institute of Clinical Radiology, Ludwig-Maximilians-Universität München, Marchioninistrasse 15, 81377 Munich, Germany

² Department of Radiology, Vrije Universiteit Brussel, Laarbeeklaan 101, 1090 Brussels, Belgium

E-mail: Steven.Sourbron@med.uni-muenchen.de

Received 27 June 2006, in final form 27 October 2006

Published 29 December 2006

Online at stacks.iop.org/PMB/52/429

Abstract

Quantification of haemodynamic parameters with a deconvolution analysis of bolus-tracking data is an ill-posed problem which requires regularization. In a previous study, simulated data without structural errors were used to validate two methods for a pixel-by-pixel analysis: standard-form Tikhonov regularization with either the L-curve criterion (LCC) or generalized cross validation (GCV) for selecting the regularization parameter. However, problems of image artefacts were reported when the methods were applied to patient data. The aim of this study was to investigate the nature of these problems in more detail and evaluate strategies of optimization for routine application in the clinic. In addition we investigated to which extent the calculation time of the algorithm can be minimized. In order to ensure that the conclusions are relevant for a larger range of clinical applications, we relied on patient data for evaluation of the algorithms. Simulated data were used to validate the conclusions in a more quantitative manner. We conclude that the reported problems with image quality can be removed by appropriate optimization of either LCC or GCV. In all examples this could be achieved with LCC without significant perturbation of the values in pixels where the regularization parameter was originally selected accurately. GCV could not be optimized for the renal data, and in the CT data only at the cost of image resolution. Using the implementations given, calculation times were sufficiently short for routine application in the clinic.

1. Introduction

Bolus-tracking experiments are applied both in MRI (e.g. Sorensen and Reimer (2000)) and in CT (e.g. Hoeffner *et al* (2004)) for the measurement of haemodynamic parameters such as tissue blood flow. The experiment proceeds by a rapid intravenous injection of a contrast

agent (a bolus), after which the contrast concentrations $C_T(t)$ in the tissue are measured as a function of time in a region of interest. Of particular interest for the study presented in this paper are imaging methods, where a function $C_T(t)$ is measured for every pixel in the field of view.

For a quantitative analysis, the data can be processed either by modelling the tissue architecture, or by a model-independent deconvolution approach (Jacquez 1985, Lassen and Perl 1979). The latter method is the focus of this paper. It requires a measurement of the contrast concentrations $C_A(t)$ inside an artery feeding the region of interest (the arterial input function, or AIF). The principles of indicator-dilution theory for linear and stationary systems (Lassen and Perl 1979) then lead to the following relation, where $*$ denotes convolution:

$$C_T(t) = C_A(t) * \mathcal{I}(t). \quad (1)$$

The unknown function $\mathcal{I}(t)$ is referred to as the impulse response function (IRF), and the procedure of calculating the IRF from $C_T(t)$ and $C_A(t)$ as deconvolution.

Since equation (1) is valid for any system that is both linear and stationary, a deconvolution analysis is physically and mathematically meaningful for all such systems. However, the extraction of exact physiological parameters from the IRF is not always straightforward. The fact is that the maximum of the IRF equals the blood flow to the tissue (usually expressed in units of $\text{ml}/100 \text{ g min}^{-1}$), provided the contrast concentrations are accurately quantified (Duhamel *et al* 2006) and the AIF is measured inside a blood vessel close to the tissue (Calamante *et al* 2000). Under the same conditions, the ratio of the time-integral to the maximum of the IRF is the mean transit time of the tracer. Additional parameters can be extracted for more complicated tissue types, but a detailed discussion of such issues and possible systematic error falls outside the scope of this paper (e.g. see Cenic *et al* (2000) and Dujardin *et al* (2005) for a discussion in tumours and in the kidney, respectively).

From a numerical perspective, deconvolution is an ill-posed problem, which means that it requires some form of regularization in order to extract a physically acceptable solution (Hansen 1998). Since a large number of regularization methods are available, this raises the question as to which approach is optimal in the context of bolus-tracking. The issue has been studied extensively in MRI, in the context of T2*-based perfusion measurements for applications of acute stroke. An early systematic comparison of methods (Østergaard 1996a, 1996b) led to the widespread use of a regularization method known as truncated singular value decomposition. The method is however typically applied with a fixed regularization parameter, which severely restricts its scope of application (Liu *et al* 1999, Murase *et al* 2001, Sourbron *et al* 2004b, Carpenter *et al* 2006).

Two strategies for selecting the regularization parameter in an objective manner, the L-curve criterion (LCC) and generalized cross validation (GCV), are well known in the literature on discrete inverse problems (Hansen 1998) and in a number of applications other than medical imaging (Corbard *et al* 1998, Farquharson and Oldenburg 2004). In Jerosch-Herold *et al* (2002), LCC was combined with an alternative regularization procedure, standard-form Tikhonov regularization (SFTR), for the deconvolution of cardiac data on a regional basis. In Koh and Hou (2003), the same method was applied for a pixel-by-pixel deconvolution of CT bolus-tracking data of the brain. Problems with image quality were reported, and in later studies an alternative method for parameter-choice was proposed (Koh *et al* 2004). In Sourbron *et al* (2004a, 2004b) simulations of T2*-data and a single clinical case were used to compare existing strategies. The simulated data led to the conclusion that SFTR with GCV or LCC were most suitable out of the alternatives investigated. However, in application to patient data problems of image quality were also apparent.

The origin of the problems with image quality in the use of LCC or GCV is not entirely clear, but may be related to structured errors in the data (Hansen 1992), to low SNR (Sourbron *et al* 2004b), or both. It is the aim of this study to investigate the nature of these problems in more detail and evaluate strategies to optimize SFTR with GCV or LCC for routine application in a broad range of clinical applications. More precisely, we aim to derive a practical and model-independent deconvolution method for bolus-tracking data, which produces parametric maps in acceptable calculation times without intervention of an expert user (Sourbron *et al* 2005).

2. Theory

A concise overview of regularization techniques, as well as methods for selecting the regularization parameter, can be found in Hansen (1998). Here we briefly introduce the methods evaluated in this study in order to unambiguously fix notations and definitions used in the text.

Since the data C_T and C_A can only be measured at n discrete time points t_0, t_1, \dots , equation (1) must be discretized before it can be applied to measured data (Smith *et al* 2004). After discretization it assumes the form of a matrix equation $\mathbf{B} = \mathbf{A}\mathbf{X}$. The n -element vector \mathbf{B} is defined as $B_i = C_T(t_i)$, and the $n \times n$ matrix \mathbf{A} depends on the values $C_A(t_i)$ in a manner dependent on the discretization scheme. The matrix equation is usually interpreted more robustly as a least-squares problem:

$$\min_{\mathbf{X}} \|\mathbf{A}\mathbf{X} - \mathbf{B}\|_2. \quad (2)$$

An important tool for solving and characterizing least-squares problems is the *singular value decomposition* (SVD) of a matrix:

$$\mathbf{A} = \mathbf{U} \text{Diag}(\sigma_1, \sigma_2, \dots, \sigma_n) \mathbf{V}^T. \quad (3)$$

Here \mathbf{U} and \mathbf{V} are orthogonal matrices holding the left and right *singular vectors* of \mathbf{A} , respectively. The diagonal elements σ_i are the *singular values* of the matrix. They are always positive and conventionally ordered in decreasing order. We will use the symbol σ to denote the array with elements σ_i .

If $\text{rank}(\mathbf{A}) = k$, then the unique minimum-norm solution to the least-squares problem (2) is given in terms of the SVD by

$$\mathbf{X} = \mathbf{V} \text{Diag}(1/\sigma_1, \dots, 1/\sigma_k, 0, \dots, 0) \mathbf{U}^T \mathbf{B}. \quad (4)$$

For deconvolution, the least-squares problem (2) is an example of an ill-posed problem, and the solution must be regularized in order to extract meaningful results. A classical approach is *standard-form Tikhonov regularization* (SFTR), which proceeds by adding the 2-norm of the solution as a quadratic constraint to the problem (2):

$$\min_{\mathbf{X}} \{ \|\mathbf{A}\mathbf{X} - \mathbf{B}\|_2^2 + \mu^2 \|\mathbf{X}\|_2^2 \}. \quad (5)$$

The *regularization parameter* μ is arbitrary *a priori*, and determines the weight of the regularizing term. In this text, we follow the convention to express numerical values for μ relative to the largest singular value σ_1 . In order to avoid confusion we will use the notation $\hat{\mu}$ for this normalized regularization parameter: $\hat{\mu} = \mu/\sigma_1$. For a given μ , the solution \mathbf{X}_μ can be expressed analytically as follows:

$$\mathbf{X}_\mu = \mathbf{V} \text{Diag} \left(\frac{\sigma_1}{\mu^2 + \sigma_1^2}, \dots, \frac{\sigma_n}{\mu^2 + \sigma_n^2} \right) \mathbf{U}^T \mathbf{B}. \quad (6)$$

The solution depends to a large extent on the value of the parameter μ . If μ is chosen too large, the solution is overregularized and may have lost all detailed structure. If μ is chosen too small the solution is underregularized, i.e. dominated by high-frequency contributions with large amplitudes. Hence no regularization method is complete without a proper procedure for choosing the regularization parameter.

Generalized cross validation (GCV) is a parameter-choice method based on the premise that the solution vector \mathbf{X}_μ should predict missing data values. A procedure of leave-one-out cross-validation leads to the following cost function (Wahba 1977):

$$\mathcal{G}(\mu) = \frac{\|\mathbf{A}\mathbf{X}_\mu - \mathbf{B}\|_2^2}{\text{trace}(\mathbf{I} - \mathbf{A}\mathbf{A}_\mu^\#)^2}. \quad (7)$$

Here \mathbf{I} is the $n \times n$ identity matrix, and $\mathbf{A}_\mu^\#$ is defined by the equation $\mathbf{X}_\mu = \mathbf{A}_\mu^\# \mathbf{B}$. In GCV, the optimal value for μ is found by minimizing the cost function $\mathcal{G}(\mu)$.

The *L-curve criterion* (LCC) is a method based on the premise that the optimal value of μ expresses a compromise between the residual norm $\rho(\mu) = \|\mathbf{A}\mathbf{X}_\mu - \mathbf{B}\|_2$ and the solution norm $\eta(\mu) = \|\mathbf{X}_\mu\|_2$. A plot of $\ln \eta$ versus $\ln \rho$ will often reveal a characteristic L-shaped curve, the ‘corner’ of which is assumed to represent the point of optimal balance between both quantities (Hansen 1992). The optimal regularization parameter is found by locating the minimum of the curvature $\mathcal{L}(\mu)$ of the L-curve.³ Simplifying notations with $\hat{\rho} = \ln \rho$ and $\hat{\eta} = \ln \eta$ we can write the curvature as

$$\mathcal{L}(\mu) = \frac{\hat{\rho}'\hat{\eta}'' - \hat{\eta}'\hat{\rho}''}{((\hat{\eta}')^2 + (\hat{\rho}')^2)^{3/2}}. \quad (8)$$

In this study, we assume the convention that derivations are taken with respect to μ .

3. Methods

3.1. Study setup

Simulated data were included in the study in order to provide an absolute measure to evaluate the results. We simulated T2-weighted data of the brain, with errors due to discretization and noise alone. For details on the simulation setup we refer to Sourbron *et al* (2004a, 2004b). For this study we used simulations of grey matter tissue with an exponential residue function, measured at a fixed temporal resolution of 1 s but with variable amounts of noise. As a measure for the noise level we use the signal-to-noise ratio at maximum concentration, a quantity denoted in this text as SNR. In order to get an estimate of the calculation error, simulations were typically performed 1000 times. For each simulation i , the maximum F_i of the calculated IRF was determined and compared to the maximum F of the exact IRF. Writing F^P for the P th percentile of the data vector $\{F_i | i = 1, \dots, 1000\}$, we derived measures for the systematic and random calculation errors as follows:

$$\text{systematic relative error} = (F^{50} - F)/F \quad (9)$$

$$\text{random relative error} = \frac{1}{2}(F^{95} - F^{05})/F. \quad (10)$$

Since it is impractical to simulate all manner of structured error that may appear in clinical data, the results from the simulations were complemented with those obtained from patient data. In order to guarantee the generality of our conclusions, we built a database with a small number of clinical cases from a wide variety of applications. We included data from two

³ The curvature is conventionally defined so that the *maximum* rather than the minimum is to be located. Here we prefer the alternative, so that GCV and LCC are both solved by a procedure of minimization.

modalities (MRI and CT), three organs (brain, breast and kidney), two pathologies (tumour and stroke) as well as volunteer studies, and different injection schemes for the bolus (see below for details). Both worst and best case data were included, to ensure that the selected data are representative of what may be encountered in clinical practice (see below for details).

With patient data, no absolute reference is available to quantify the accuracy of the calculations. Hence the outcome was evaluated on the basis of physical arguments such as continuity of the images, the characteristics of the IRF (which should be a decreasing function), or comparison of the calculated parameters in anatomical regions to gold-standards (when available). The latter criterion is to a certain extent quantitative, but it does not provide an absolute reference (e.g. see Dujardin *et al* (2005)). One reason is that the presence of systematic error can generally not be excluded, in which case observed discrepancies with a gold-standard are not due to calculation errors alone. A second reason is that there is often a large range of normality in parameters such as blood flow, so that an observed deviation from a typical gold-standard value does not necessarily entail a measurement error. For this study we used reference values only as an order-of-magnitude estimate: since neither systematic error nor normal variations can explain deviations of one or more orders of magnitude, such results are likely to arise from calculation errors.

The study was set up in four stages.

- (i) The first stage consisted of an exploratory study, where data in the patient database were processed with the algorithm used in previous simulations (Sourbron *et al* 2004b). The cost functions for a limited number of pixels with suspected calculation errors were studied in detail in order to identify the source of the problem. A procedure for optimization was proposed on the basis of these observations, and simulations were used to validate the proposal and compare it to the original approach.
- (ii) In a second stage the proposed strategy was implemented for application on a pixel-by-pixel basis, and it was investigated whether the implementation of the proposed deconvolution method could be designed so that calculation times were sufficiently short for clinical routine. Simulated data were used to quantify the calculation times as a function of the size of the dataset.
- (iii) Third, the final algorithms were applied systematically to all patient data in the database. Results were evaluated by searching maps of the maximum in the IRF (i.e. the physiological parameter of blood flow) for discontinuities or structures that cannot be explained by anatomy or pathology, and for pixels with unphysical blood flow values. When such regions were identified, the maximum maps were compared to maps of the regularization parameter to assess whether suspected pixel values may be due to erroneous selection of the regularization parameter. For a selected number of such pixels the structure of the cost function was plotted in order to identify the source of the problem and arrive at a classification and description of parameter-choice artefacts.
- (iv) Finally, an approach to reduce the occurrence of described artefacts was proposed and implemented, and the data were re-evaluated with this improved algorithm. Results were compared to those obtained in the previous phase, both qualitatively using patient data, and quantitatively using simulations.

3.2. Included data

All MRI scans were obtained on a 1.5 T Philips Intera scanner. CT data were measured on a four-row multisection Siemens Volume Zoom. In the MRI-investigations the bolus was flushed with 15 ml of saline injected at the same rate as the bolus. An overview of the data included in the study is provided in the following list.

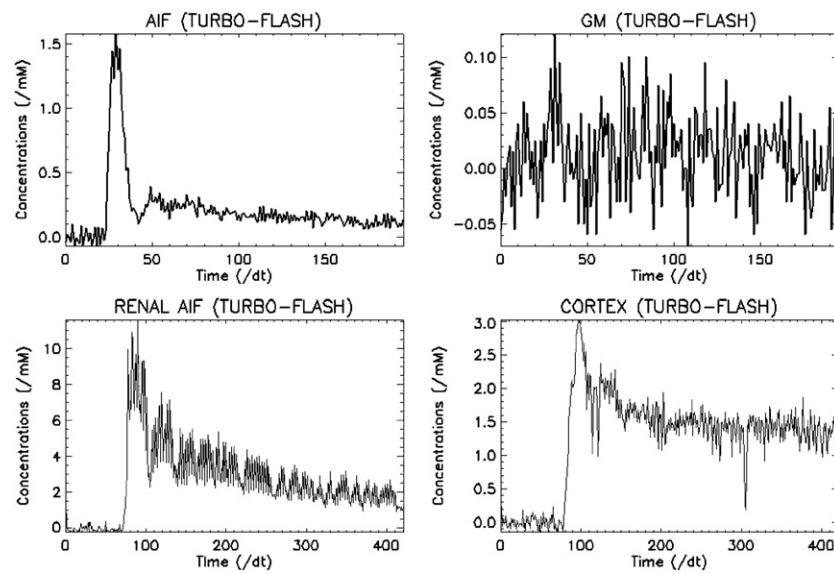


Figure 1. An example of TURBO-FLASH data for the brain (top row) and for the kidney (bottom row). The left column shows the AIF, the right column gives a typical example of a single voxel concentration time course measured in grey matter (top) and renal cortex (bottom).

- (i) T2*-weighted GE-EPI images of the brain (18 slices, 40 dynamics, 128×128 matrix, TR 951 ms, TE 30 ms, flip angle 40° , FOV 260×260 mm, slice thickness 6 mm, slice gap 6 mm). 40 ml of Gd-DTPA was injected at 8 ml s^{-1} (three stroke cases).
- (ii) MR-PRESTO images of the brain (22 slices, 40 dynamics, 128×128 matrix, TR 23.2 ms, TE 9 ms, flip angle 7° , FOV 220×220 mm, slice thickness 6 mm, slice gap 6 mm). 40 ml of Gd-DTPA was injected at 8 ml s^{-1} (two stroke cases).
- (iii) T1-weighted TURBO-FLASH images of the brain (three slices, 250 dynamics, 128×90 matrix—reconstructed at 256×256 , time resolution 1.1 s, TI 240 ms, TR 4.60 ms, TE 2.3 ms, flip angle 50° , FOV 200×250 mm, slice thickness 6 mm, slice gap 1 mm). 10 ml of Gd-DTPA was injected at 2 ml s^{-1} . Included three tumour cases (Sourbron *et al* 2005).
- (iv) T1-weighted TURBO-FLASH images of the kidney (one slice, 500 dynamics, 128×90 matrix—reconstructed at 256×256 , time resolution 0.31 s, TI 180 ms, TR 4.33 ms, TE 2.2 ms, flip angle 50° , FOV 346×435 mm, slice thickness 4 mm). 20 ml of Gd-DTPA was injected at 2 ml s^{-1} . Included three volunteer studies (Dujardin *et al* 2005).
- (v) T1-weighted TURBO-FLASH images of the breast (one slice, 600 dynamics, 128×90 matrix—reconstructed at 256×256 , time resolution 0.31 s, TI 196 ms, TR 4.9 ms, TE 2.4 ms, flip angle 50° , FOV 230×183 mm, slice thickness 6 mm). 20 ml of Gd-DTPA was injected at 2 ml s^{-1} . Included three breast tumours studies (Makkat *et al* 2005).
- (vi) CT perfusion of the brain (two or four slices, 40 dynamics, 512×512 matrix, temporal resolution 1 s, 80 kV, 209 mA s, FOV 200×200 mm, slice thickness 5 mm). 40 ml of non-ionic iodinated contrast was injected at 8 ml s^{-1} or at 4 ml s^{-1} . Included three tumour cases (Sourbron *et al* 2005) and three stroke cases.

Figure 1 illustrates that a broad spectrum of data characteristics is included: the T1-weighted brain data are characterized by a stable arterial input function but small SNR in (normal) brain tissue; the kidney data have good SNR, but the input function is severely

distorted by inflow fluctuations (Dujardin *et al* 2005), and the tissue data are affected by motion artefacts.

3.3. Post-processing

Simulated and patient data were processed off-line with in-house built software (PMI 0.2, Sourbron (2005)), written in IDL 5.4 (RSI, Boulder, CO). Signal-time courses were converted to contrast concentrations in a manner dependent on the modality and contrast mechanism: for the T2-weighted data, concentrations were calculated as $-\ln(S/S_0)$; for the CT data, concentrations were calculated by the signal enhancement $S - S_0$; for the T1-weighted data, concentrations were either approximated by relative signal enhancement $(S - S_0)/S_0$ (Makkat *et al* 2005), or quantified using a phantom with known T1 placed in the field of view (Dujardin *et al* 2005). In all cases, an AIF was determined by manually selecting arterial regions.

Maps were generated of the maximum of the IRF (the blood flow), the time-integral of the IRF (the volume of distribution) and the ratio of both (the mean transit time). In addition, maps of the selected regularization parameter were generated, as well as images of the calculated functions $\mathcal{G}(\mu)$ and $\mathcal{L}(\mu)$.

4. Results

4.1. Optimization of LCC and GCV

A naive application of either LCC or GCV, where the functions $\mathcal{L}(\mu)$ or $\mathcal{G}(\mu)$ are optimized by locating the global minimum, is not acceptable for a pixel-wise analysis of bolus-tracking data. Figure 2 (top row) illustrates that maps calculated in this manner lead to unphysical values for the perfusion parameters in some (or most) of the pixels. The origin of the problem is exposed by closer inspection of the functions $\mathcal{L}(\mu)$ or $\mathcal{G}(\mu)$ (figure 2, bottom row). The curvature of the L-curve typically has multiple well pronounced local minima, the largest of which may appear anywhere on the μ -axis. The structure of the GCV cost function is generally better defined. Nearly always there is a global minimum at the upper end of the μ interval, but other minima may appear at very low values of μ . The GCV-minima are more flat than those of LCC, typically spanning 1–2 orders of magnitude in μ .

Correlating the plots in figure 2 with the maps shows that results are unphysical exactly in those pixels where the global minimum lies at low values for μ . In previous studies (Sourbron *et al* 2004a, 2004b) we applied an ad hoc solution, where the functions $\mathcal{L}(\mu)$ or $\mathcal{G}(\mu)$ were optimized by selecting the global minimum on a restricted interval $10^{-3} < \hat{\mu} < 1$. Inspection of simulated and patient data included in this study confirmed that this approach is acceptable for GCV, since the physical minima in $\mathcal{G}(\mu)$ appear at $\hat{\mu} > 10^{-3}$, and the unphysical minima at $\hat{\mu} \ll 10^{-3}$. For LCC on the other hand, multiple peaks may appear in the window $10^{-3} < \hat{\mu} < 1$, particularly in regions with low SNR. This leads to underregularized solutions in such regions, an effect previously observed in simulations with varying SNR-values (Sourbron *et al* 2004b).

Since pixels with various levels of SNR may appear within a single image, selecting a different lower bound on μ for each dataset is not an acceptable solution. Detailed inspection of the data included in this study suggested that the optimum in $\mathcal{L}(\mu)$ could be identified as the local minimum nearest to the upper bound $\hat{\mu} = 10$. This is not immediately obvious: for many pixels with low SNR, this local minimum is very weakly defined and/or appears at positive values for the curvature. In that case, the ‘L’-curve is not even convex at this point,

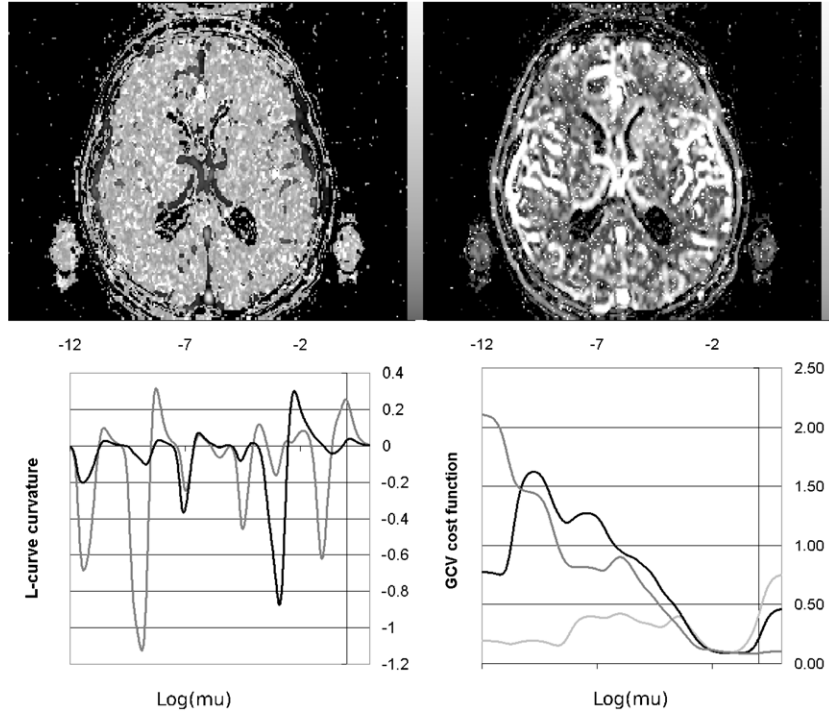


Figure 2. On the top row, maps of the maximum of the impulse response function for the TURBO-FLASH data in the brain with μ chosen at the global minimum in the cost function for LCC (left) and GCV (right). On the bottom row, plots of LCC curvatures (left) and GCV cost functions (right) for two (resp. three) pixels in the image.

which appears to contradict the principles of the approach. Nevertheless, comparison with alternative choices for the optimum suggested that even in such cases, parametric values were realistic only when the local minimum nearest to $\hat{\mu} = 10$ was selected. Note that for GCV, this procedure is equivalent to selecting a global minimum on the restricted interval. Hence we can apply the same optimization procedure for both LCC and GCV.

For a practical implementation, we define a vector μ with n_μ possible values for μ , distributed logarithmically between the values $\sigma_1 \hat{\mu}_{\min}$ and $\sigma_1 \hat{\mu}_{\max}$:

$$\mu_k = \sigma_1 \hat{\mu}_{\min} \left(\frac{\hat{\mu}_{\max}}{\hat{\mu}_{\min}} \right)^{\frac{k-1}{n_\mu-1}} \quad k = 1, \dots, n_\mu. \quad (11)$$

For each pixel, an n_μ -element vector \mathbf{C} is calculated by $C_k = \mathcal{G}(\mu_k)$ for GCV and $C_k = \mathcal{L}(\mu_k)$ for LCC. This vector is then optimized by starting at $k = n_\mu - 1$, and moving towards lower values until a local minimum is found. For pixels that do not have a local minimum, the default value μ_{\max} is returned:

Algorithm OPTIMIZE(μ , \mathbf{C})

- (i) Set $k = n_\mu - 1$
- (ii) While $C_k \geq C_{k-1}$ or $C_k \geq C_{k+1}$ do
 - (a) Set $k = k - 1$
 - (b) If $k = 1$ then return μ_{\max}
- (iii) Return μ_k .

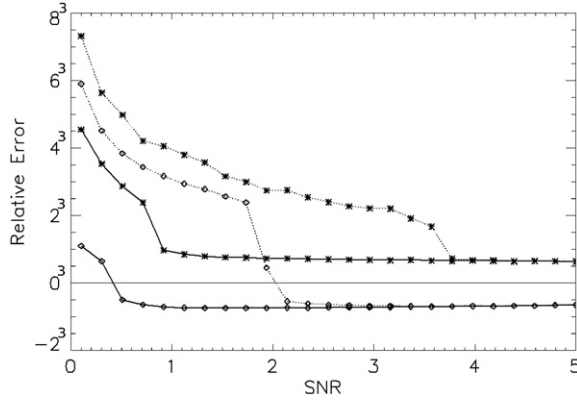


Figure 3. Random (*) and systematic (◇) error for two different optimization methods applied to LCC: selecting a local minimum with the algorithm OPTIMIZE() (full line) and selecting the global minimum in an interval $10^{-3} < \hat{\mu} < 10$ (dotted line). For reasons of clarity, the errors are plotted on an exponential scale.

For all studies, we used the values $\hat{\mu}_{\min} = 10^{-3}$, $\hat{\mu}_{\max} = 10$ and $n_{\mu} = 100$. The lower bound was set to this value since inspection of first results showed no occurrence of lower values for the optimal μ . The same results also showed that a gridsize of $n_{\mu} = 100$ was sufficient to resolve the structure of the cost functions accurately.

The simulations confirm that results calculated with OPTIMIZE() are more robust and more accurate than those obtained by selecting a global maximum on a restricted interval (figure 3). The figure shows that both algorithms produce identical results when the data are sufficiently accurate, in this case at higher levels of SNR. In this regime, the peak in the LCC curvature selected by OPTIMIZE() is also the largest peak on the interval $10^{-3} < \hat{\mu} < 10$. When the data accuracy is reduced (i.e. by reducing SNR in the simulations) this ‘physical’ peak in the LCC curvature is reduced in amplitude, and ‘unphysical’ peaks at lower values of μ are amplified. In this case the solutions obtained by selection of a global peak are increasingly underregularized, leading to an amplification of both random and systematic error. Note that the same effect eventually appears with OPTIMIZE() as well, but only at $\text{SNR} < 0.5$. In this regime the data are fully dominated by the noise, and the physical peak in the curvature disappears altogether.

4.2. Algorithms

In order to maximally reduce the calculation time in the implementation of SFTR with LCC or GCV for imaging, we first rewrote formulae (7) and (8) and separated the contribution of the pixel data \mathbf{B} from that of the arterial input function (which is common to all pixels). Using equation (6) in (7), and expanding the norm we can rewrite the formula for the GCV cost function as follows (\mathbf{U}_i is column i of matrix \mathbf{U}):

$$\mathcal{G}(\mu) = \sum_{i=1}^n g_i(\mu, \sigma) (\mathbf{U}_i^T \mathbf{B})^2. \quad (12)$$

Here $g_i(\mu, \sigma)$ is defined as

$$g_i(\mu, \sigma) = \left(\sum_{j=1}^n \frac{\mu^2 + \sigma_i^2}{\mu^2 + \sigma_j^2} \right)^{-2}. \quad (13)$$

This quantity does not depend on the pixel data \mathbf{B} , so it can be calculated outside the main loop. For LCC it is convenient to use equations (6) in (8) and reduce the formula for the curvature as follows:

$$\mathcal{L}(\mu, m_0, m_1, m_2) = 2 \frac{m_1 m_0}{m_2} \frac{\mu^2 m_2 m_0 + 2\mu m_1 m_0 + \mu^4 m_1 m_2}{(\mu^4 m_1^2 + m_0^2)^{3/2}}. \quad (14)$$

The quantities m_0, m_1, m_2 are defined as $m_0 = \rho^2$, $m_1 = \eta^2$ and $m_2 = m'_1$. They can be calculated as

$$m_j = \sum_{i=1}^n l_j(\mu, \sigma_i) (\mathbf{U}_i^T \mathbf{B})^2 \quad (15)$$

with the definitions:

$$l_0(\mu, \sigma) = \left(\frac{\mu^2}{\sigma^2 + \mu^2} \right)^2 \quad (16)$$

$$l_1(\mu, \sigma) = \left(\frac{\sigma}{\sigma^2 + \mu^2} \right)^2 \quad (17)$$

$$l_2(\mu, \sigma) = \frac{-4\mu\sigma^2}{(\sigma^2 + \mu^2)^3}. \quad (18)$$

The quantities l_j play a role analogous to g_i in equation (12): they do not depend on the pixel data, so they can be calculated outside the main loop.

The result is encoded in the algorithm DECONVOLVE() presented below. We define the number of pixels as n_p and assume the pixel concentrations are organized into a $n_p \times n_t$ matrix \mathbf{B} . The algorithm DECONVOLVE() takes \mathbf{A} and \mathbf{B} as inputs. The other inputs are the three numbers which define the grid over which $\mathcal{G}(\mu)$ or $\mathcal{L}(\mu)$ are optimized (equation (11)). Upon return, the matrix \mathbf{B} holds the values of the discretized impulse response function for every pixel.

Algorithm DECONVOLVE($\mathbf{B}, \mathbf{A}, \hat{\mu}_{\min}, \hat{\mu}_{\max}, n_\mu$)

- (i) Calculate the SVD $\mathbf{U}, \sigma, \mathbf{V}$ of the matrix \mathbf{A}
- (ii) Calculate $\mathbf{B} = \mathbf{U}^T \mathbf{B}$
- (iii) Execute $\mathbf{O} = (\text{LCC or GCV}) \text{ REGPAR}(\mathbf{B}, \sigma, \hat{\mu}_{\min}, \hat{\mu}_{\max}, n_\mu)$
- (iv) $\forall p, i$ calculate $B_{pi} = B_{pi} \sigma_i / (\sigma_i^2 + O_p^2)$
- (v) Calculate $\mathbf{B} = \mathbf{V} \mathbf{B}$.

Expressions (6), (13) and (15) demonstrate explicitly that the solution \mathbf{X}_μ and the functions $\mathcal{G}(\mu)$ and $\mathcal{L}(\mu)$, depend upon the pixel data only through $\mathbf{U}^T \mathbf{B}$. Hence this matrix–vector product can be calculated as a first step. The algorithm makes use of one of the subroutines LCCREGPAR() or GCVREGPAR(), which return an n_p -element vector \mathbf{O} holding the values of the optimal regularization parameter.

Assuming that the matrix–vector product $\mathbf{B} = \mathbf{U}^T \mathbf{B}$ has been calculated, the GCV parameter-choice method can be implemented as follows (we write \mathbf{C}_p for column p of matrix \mathbf{C}).

Algorithm GCVREGPAR ($\mathbf{B}, \sigma, \hat{\mu}_{\min}, \hat{\mu}_{\max}, n_\mu$)

- (i) Create a vector μ with equation (11)
- (ii) Create an $n_p \times n_t$ matrix \mathbf{C} with $C_{pt} = B_{pt}^2$
- (iii) Create an $n_\mu \times n_t$ matrix \mathbf{G} by $G_{ki} = g_i(\mu_k, \sigma)$ (equation (13))
- (iv) $\forall p$ set $O_p = \text{GCVOPTIMIZE}(\mu, \mathbf{G}, \mathbf{C}_p)$, and return \mathbf{O} .

The loop over all pixels p is a modification of the algorithm OPTIMIZE(), which guarantees that the values of $\mathcal{G}(\mu)$ are calculated only until the local minimum is reached (write \mathbf{G}_k for column k of matrix \mathbf{G}):

Algorithm GCVOPTIMIZE ($\mu, \mathbf{G}, \mathbf{C}$)

- (i) Set $k = n_\mu - 1$
- (ii) For $j = -1, 0, 1$ set $G_j = \mathbf{G}_{k+j}^T \mathbf{C}$
- (iii) While $G_0 \geq G_{-1}$ or $G_0 \geq G_1$ do
 - (a) Set $k = k - 1$
 - (b) If $k = 1$ then return μ_{\max}
 - (c) Set $G_1 = G_0, G_0 = G_{-1}$ and $G_{-1} = \mathbf{G}_{k-1}^T \mathbf{C}$
- (iv) Return μ_k .

The algorithm to calculate the LCC regularization parameter is entirely analogous to that for GCV.

Algorithm LCCREGPAR ($\mathbf{B}, \sigma, \hat{\mu}_{\min}, \hat{\mu}_{\max}, n_\mu$)

- (i) Create a vector μ with equation (11)
- (ii) Create an $n_p \times n_t$ matrix \mathbf{C} with $C_{pt} = B_{pt}^2$
- (iii) Create an $n_\mu \times n_t \times 3$ matrix \mathbf{L} by $L_{kij} = l_j(\mu_k, \sigma_i)$ (equations (16), (17) and (18))
- (iv) $\forall p$ set $O_p = \text{LCCOPTIMIZE}(\mu, \mathbf{L}, \mathbf{C}_p)$, and return \mathbf{O} .

Again the pixel-loop is an adaptation of the algorithm OPTIMIZE(). To simplify notations, we write $\mathbf{L}_{k,j}$ for the column vector with elements $\{L_{kij} | i = 1, \dots, n_t\}$:

Algorithm LCCOPTIMIZE ($\mu, \mathbf{L}, \mathbf{C}$)

- (i) Set $k = n_\mu - 1$
- (ii) For $j = -1, 0, 1$ set $L_j = \mathcal{L}(\mu_{k+j}, \mathbf{L}_{k+j,0}^T \mathbf{C}, \mathbf{L}_{k+j,1}^T \mathbf{C}, \mathbf{L}_{k+j,2}^T \mathbf{C})$.
- (iii) While $L_0 \geq L_{-1}$ or $L_0 \geq L_1$ do
 - (a) Set $k = k - 1$
 - (b) If $k = 1$ then return μ_{\max}
 - (c) Set $L_1 = L_0, L_0 = L_{-1}$ and $L_{-1} = \mathcal{L}(\mu_{k-1}, \mathbf{L}_{k-1,0}^T \mathbf{C}, \mathbf{L}_{k-1,1}^T \mathbf{C}, \mathbf{L}_{k-1,2}^T \mathbf{C})$
- (iv) Return μ_k .

Figure 4 simulates the calculation times as a function of the number of dynamics for a typical slice (PC workstation, 2.5 GHz processor, 512 MB memory). Note that GCV is faster than LCC, and that the calculation time increases with SNR. The reason is that with more accurate data the minimum of the cost functions lies at smaller values of μ , so that the algorithm OPTIMIZE()—which starts its search at the upper value for μ —takes longer to find the minimum. This also implies that the dependence on SNR could be reversed by setting the initial choice for μ at the lower bound. Other strategies for reducing the calculation time would be to reduce the value for n_μ (here set at 100) or restricting the number of pixels by calculating only a region of interest within the slice. The latter strategy was applied to the patient data, which led to calculation times below 5 min for all applications.

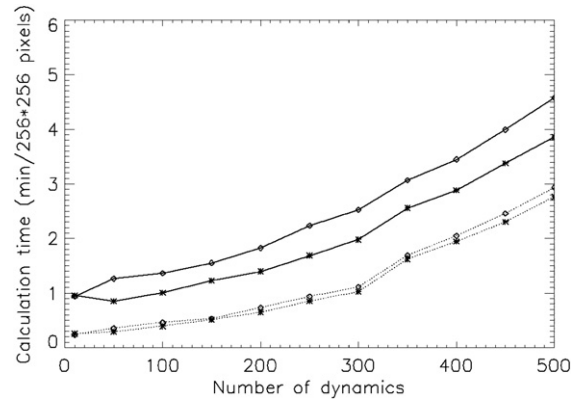


Figure 4. Calculation times with LCC (full line) and GCV (dotted line) for a slice containing 256×256 pixels. Results are given at two different levels of SNR: 20 (\diamond) and 2 (*).

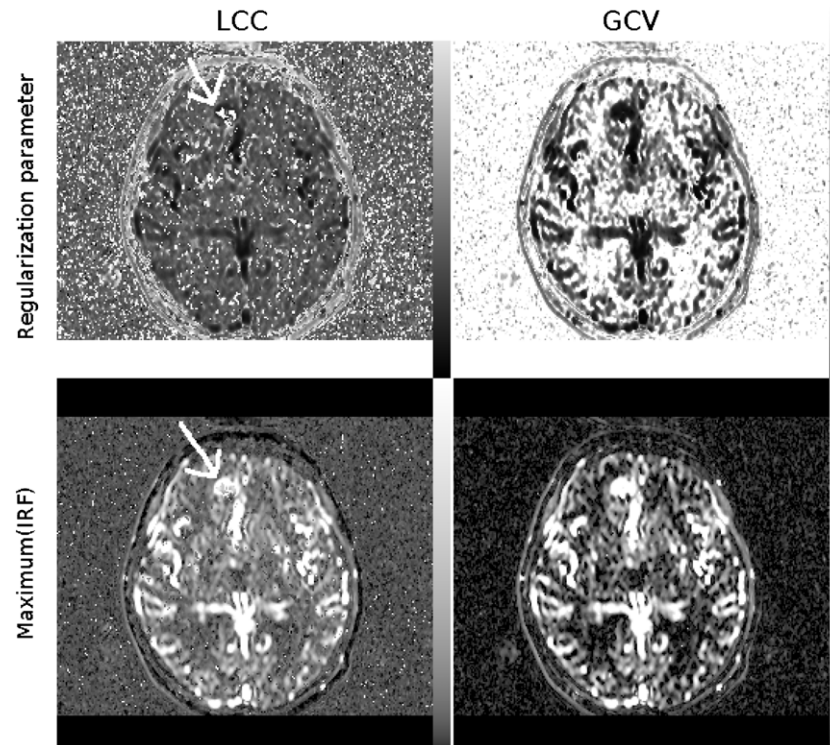


Figure 5. Maps of the regularization parameter (top row) and the maximum of the IRF (bottom row) calculated with the improved minimization of LCC (left column) and GCV (right column) on TURBO-FLASH data of the brain. Grey scale ranges from 0.0 to 0.5 (top row) and from 0.0 to $0.03 \text{ ml ml}^{-1} \text{ s}^{-1}$ (bottom row). Note the appearance of overregularized pixels on the LCC images (a relatively large cluster in the tumour edge is pointed out), which are most easily identified as hyperintense pixels on the map of μ .

4.3. Image artefacts

The results of the optimized minimization scheme are summarized in figures 5 and 6. These data are selected to illustrate the general observations. Comparison of the bottom row in

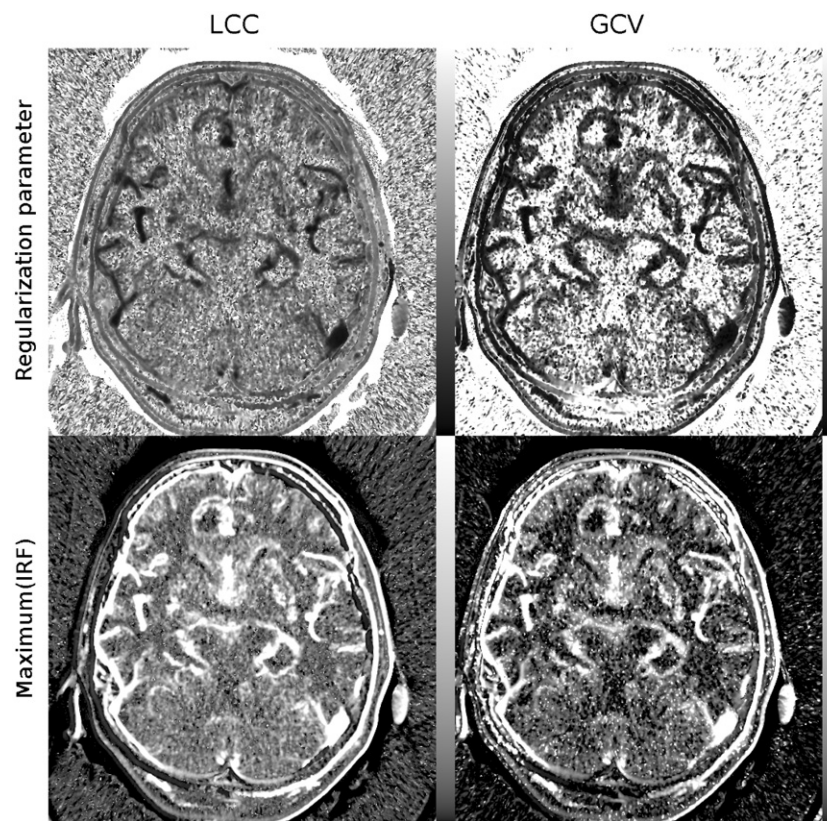


Figure 6. Maps of the regularization parameter (top row) and the maximum of the IRF (bottom row) calculated with the improved minimization of LCC (left column) and GCV (right column) on CT data of the brain. Grey scale ranges from 0.0 to 0.5 (top row) and from 0.0 to 0.05 ml ml⁻¹ s⁻¹ (bottom row). Note that both with LCC and GCV, underregularized solutions appear in the form of hyperintense pixels in the maps of the maximum in the IRF. The problem is more severe with GCV than with LCC.

figure 5 to the top row of figure 2 shows that the optimization scheme encoded in the algorithm OPTIMIZE() leads to physically acceptable values for the regularization parameter almost everywhere in the image. However, closer inspection reveals that both over- and underregularized solutions can still be found on the pixel level.

Overregularized solutions were only found when LCC was used in the TURBO-FLASH data of the brain. They appear in regions with high or low SNR, and can be recognized as clusters or individual pixels with unphysically low values on maps of the maximum of the IRF. Alternatively, this type of artefact can be detected as hyperintense pixels on images of the regularization parameter. An example is pointed out in figure 5 (see arrow), of a relatively large cluster of overregularized pixels in the tumour edge.

Underregularized solutions were found with both methods, but GCV is more sensitive to this problem. In the simulated data, underregularized data were encountered with GCV at all levels of SNR, but with LCC only at SNR < 0.5 (see also figures 3, 10 and discussions thereof). On the patient data the problem typically appears in regions with low SNR in the form of isolated pixels or small clusters with high maximum values (typically one to two orders of magnitude too high), or correspondingly low values on the maps of μ (figure 6).

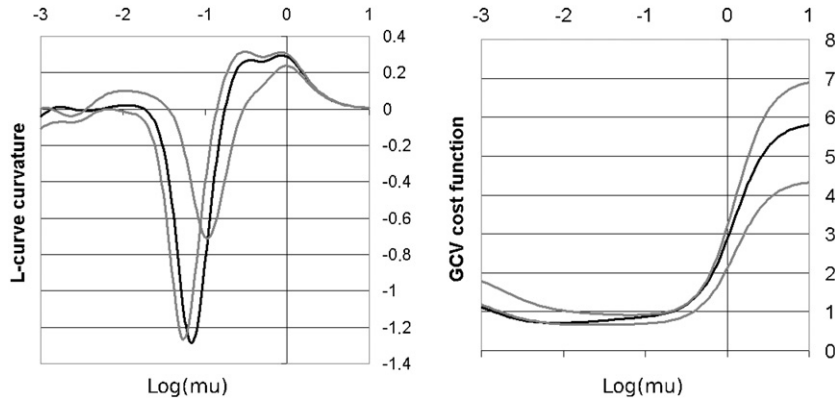


Figure 7. Plots for a pixel (black) and two neighbouring pixels (grey) illustrating the two sources of image artefacts. On the left, plots of $\mathcal{L}(\mu)$ for a pixel in the cluster of overregularized solutions pointed out in figure 5. The pixel is chosen so that one of the neighbours lies in the same cluster, but the other lies outside it. On the right, plots of $\mathcal{G}(\mu)$ for an underregularized pixel in figure 5, and two neighbours which are not underregularized.

Figure 7 illustrates the origin of over- and underregularized solutions in more detail. The plots of the curvature (left) show that all pixels have a clear convex corner in the L-curve near an appropriate value for the regularization parameter. However, for the pixels inside the overregularized cluster a small local minimum appears at higher values for μ . With the proposed optimization scheme it is this, rather than the appropriate minimum, which is selected. Underregularized solutions, on the other hand, appear in situations where the optimum is missing altogether, so that the algorithm `OPTIMIZE()` selects a local minimum at values of μ which are too low. Figure 7 (right) is an example of this effect. It is typical for GCV that the minimum in the function $\mathcal{G}(\mu)$ is flat, i.e. covers two or more orders of magnitude. In this case we observed that the pixel, where the solution is underregularized, corresponds to a local minimum at the left end of the plateau—in contrast to the neighbouring pixels. In LCC the problem arises in low SNR regions when the L-curve is flattened out to the extent that no local minimum is found in the curvature at acceptable values for μ .

4.4. Reducing artefacts

Since the underregularized pixels are generally isolated or grouped in small clusters, the problem may be removed by mixing in information from neighbouring pixels. As a straightforward solution we investigated the effect of in-slice smoothing of the cost functions prior to optimization with `OPTIMIZE()`. Mixing in the cost functions from neighbouring voxels in this manner may reintroduce an optimum in isolated pixels where there is none, but care must be taken that it does not lead to problems in sharp tissue interfaces.

Since overregularized pixels may be grouped in larger clusters, it is unlikely that this problem can be dealt with effectively by in-slice smoothing. In fact, preliminary experiments demonstrated that such an operation introduces the problem in neighbouring voxels. Reducing the values for $\hat{\mu}_{\max}$ presented a solution in some cases, but often it was found that this causes other pixels to be underregularized. On the other hand, since the correct optimum is typically very well pronounced in these regions (figure 7, left), one may hope to remove the weaker local minima by a smoothing operation along the μ -axis. A potential problem with such an approach is that weak minima in noisy pixels may be flattened as well, causing these data to be underregularized.

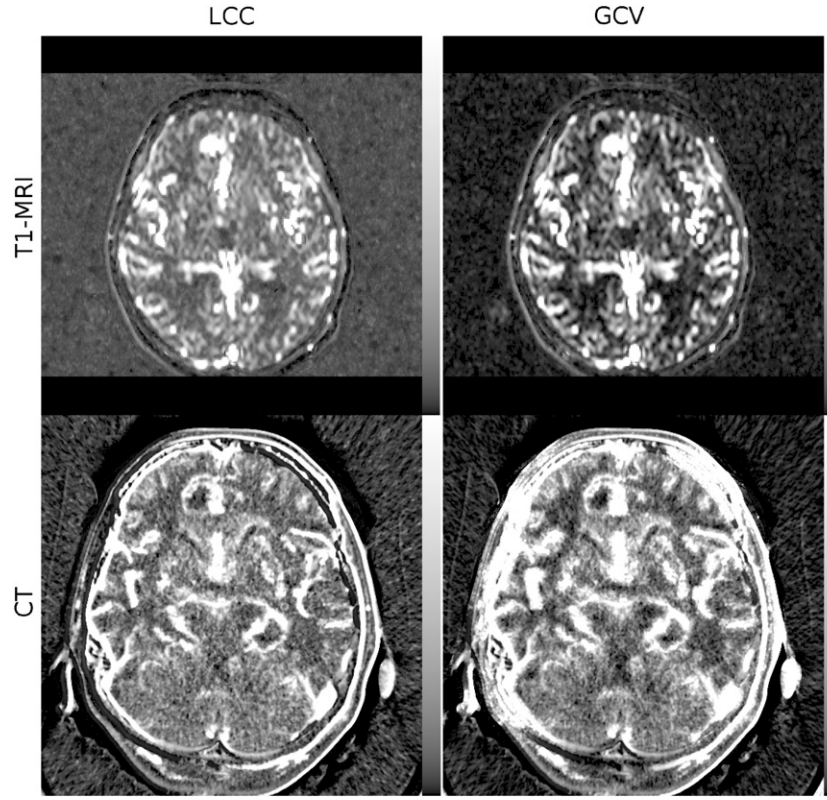


Figure 8. Same maps, grey scales and methods as in figure 5 (top row, MRI data) and figure 6 (bottom row, CT data), but with additional smoothing on the cost functions. The smoothing windows (w_s , w_μ) for these data are set to (5, 13) (top left), (3, 1) (top right), (7, 1) (bottom left) and (13, 1) (bottom right). Note that, with these settings, both over- and underregularized values disappear (compared to figures 5 and 6).

In order to evaluate these methods we modified the algorithms GCVREGPAR() and LCCREGPAR() to incorporate a uniform smoothing of $\mathcal{G}(\mu)$ or $\mathcal{L}(\mu)$. In practice this implies replacing step (iv) in both algorithms by (iv)–(vi) as follows (w_μ and w_s are user-defined values of the smoothing windows).

Algorithm GCVREGPAR⁺ (\mathbf{B} , σ , $\hat{\mu}_{\min}$, $\hat{\mu}_{\max}$, n_μ , w_μ , w_s)

- (i) Create a vector μ with equation (11)
- (ii) Create an $n_p \times n_t$ matrix \mathbf{C} with $C_{pt} = B_{pt}^2$
- (iii) Create an $n_\mu \times n_t$ matrix \mathbf{G} by $G_{ki} = g_i(\mu_k, \sigma)$ (equation (13))
- (iv) Calculate $\mathbf{C} = \mathbf{G}^T \mathbf{C}$
- (v) Uniformly smooth \mathbf{C} , first along the μ -axis with a window w_μ , then in-slice with a window w_s
- (vi) $\forall p$ set $O_p = \text{OPTIMIZE}(\mu, \mathbf{C}_p)$ and return \mathbf{O} .

The modification for LCC is entirely analogous. Note that apart from the additional smoothing step, the calculation time is increased since the cost functions are now calculated for all values of μ (step (iv)). The size of the smoothing windows (w_μ , w_s) was optimized for every application in two steps: first w_μ was increased until overregularized solutions disappeared; with this value of w_μ , we then increased w_s until underregularized solutions vanished.

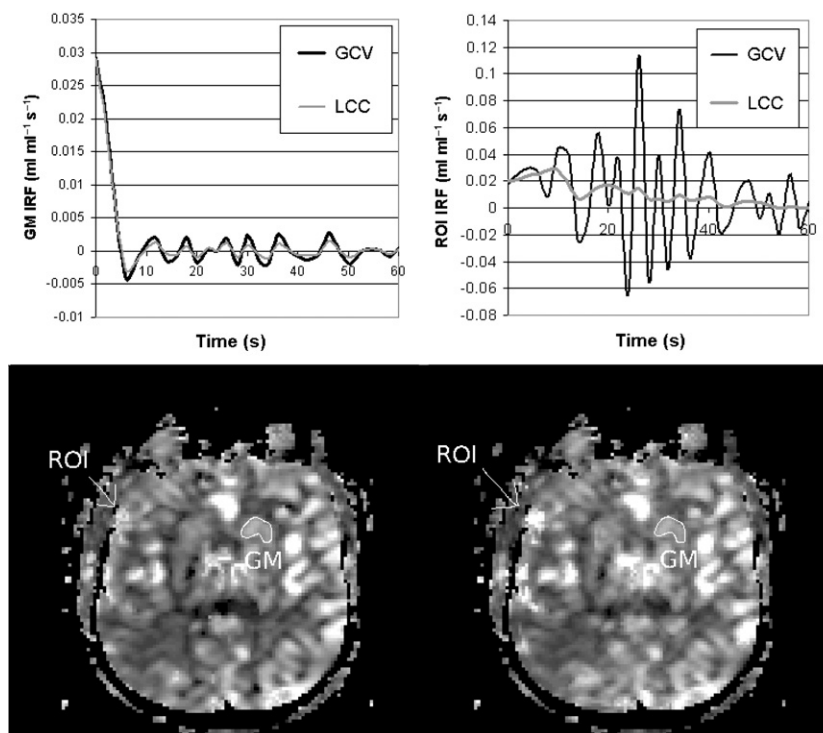


Figure 9. High-dose GE-EPI data of an acute stroke patient. On the bottom row a map of the maximum of the impulse response function calculated with LCC (left, $w_s = 3$) and GCV (right, $w_s = 5$). Grey scale ranges from 0.0 to 0.1 $\text{ml ml}^{-1} \text{s}^{-1}$ in both cases. On the top row the impulse responses calculated with both techniques and averaged over two regions of interest indicated on the maps. A grey matter ROI (GM) in the basal ganglia, and an ROI chosen in a region where LCC and GCV produced different results.

Figure 8 illustrates the effect of this additional step, for the data in figures 5 and 6. We observed that most (see below for exceptions) artefacts due to under- and overregularization could be removed when appropriate values for (w_μ, w_s) were chosen. The optimal values for (w_μ, w_s) were dependent on the application, but were fixed for various datasets measured by the same technique.

Moreover, comparing figure 8 to 5 and 6, we see that the effect of this additional step on parameter values in artefact-free regions is minimal (note that the grey scales are identical). The effect of mixing at interfaces between tissue types was clearly visible on the maps of the regularization parameter, but to a much weaker extent on the maximum-maps. An effect on image resolution is most obvious in the CT data calculated with GCV, where a relatively large window was required to remove underregularized pixels (figure 8).

One notable exception to these general observations was the GCV results in the kidney, where large regions were underregularized (Sourbron 2005). Here the proposed method of in-slice smoothing does not apply, so that the GCV method must be rejected in this application. Similar, but less obvious, problems with underregularized pixels were observed with GCV in some other applications. Figure 9 shows an example, where the problem can be detected by comparing GCV and LCC results. In most of the image, both methods produce virtually identical results (see the grey matter region). Comparing both maps we see that in some smaller subregions the GCV-values are higher. A plot of the IRF in these regions clearly

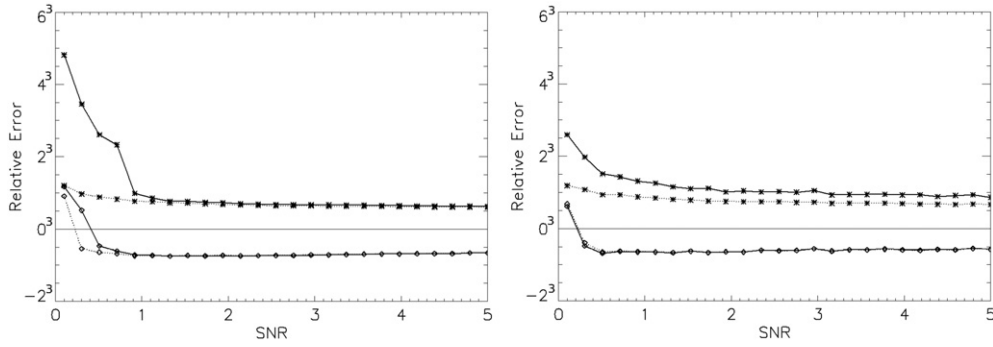


Figure 10. The effect of cost-function smoothing for LCC (left) and GCV (right) on the systematic (\diamond) and random ($*$) error. Plotted are the errors without cost-function smoothing (full line) and after uniform smoothing with a window of 3 (dotted line). For reasons of clarity, the errors are plotted on an exponential scale.

shows that the GCV-solutions are underregularized and must be rejected. Without inspection of the IRF, such errors are not immediately recognizable as image artefacts, and may lead to false interpretations of the results.

The effect of cost-function smoothing on overregularized solutions could not be verified on the simulations since we did not find evidence of such problems in the simulated data. The effect of in-slice smoothing of the cost functions on underregularized solutions is illustrated in figure 10. Note that this additional step does not affect the systematic error, except for LCC at $\text{SNR} < 0.5$. This confirms the observations made in the patient data, that in sufficiently homogeneous regions (i.e. where no sharp interfaces between tissue types are present) the effect of cost-function smoothing is to improve the robustness of the method without affecting the accuracy. In particular, figure 10 demonstrates that the effect of the smoothing step is to reduce the random error at all values of SNR where underregularized solutions are found: for GCV at all values SNR, and for LCC only at small SNR. Note also that, when the smoothing step is added, LCC and GCV produce identical random and systematic errors.

5. Discussion

The results have shown that when the appropriate optimization procedure is combined with methods of cost-function smoothing, parametric maps without obvious image artefacts can be obtained with both methods. In view of our aims to derive algorithms that are functional without the intervention of an expert user, the question remains how the values for the smoothing windows (w_s, w_μ) are to be determined. The results show that the optimal values are application dependent, but with the limited data available in the study it was possible to identify a fixed setting for each application. Whether it is feasible to fix the values of (w_s, w_μ) for a given application can only be decided conclusively when more data are available. Recent experience with data in ongoing clinical studies (Makkat *et al* 2005, Dujardin *et al* 2005) does however suggest a positive answer to the question.

Awaiting further experience, we use the values ($10^{-3}, 10, 100, 1, 1$) for the parameters ($\hat{\mu}_{\min}, \hat{\mu}_{\max}, n_\mu, w_s, w_\mu$) as defaults. When a new clinical application is initiated, an expert user optimizes those default values on the basis of inspection of a limited number of datasets. These optimized values are then fixed for all patient data acquired in the context of the same application. We note that the current study has indicated no reason for modifying the default values of $\hat{\mu}_{\min}$ or $\hat{\mu}_{\max}$. Future studies may investigate to what extent the value of n_μ can be

reduced in the interest of calculation time, without significantly altering the quantification of the parameters.

The question of a comparison between LCC and GCV was not part of the aims of this study, but the results do provide some insight into the issue. First, we observed that no unique answer can be given to this question when the overall image quality is taken as a criterion. For instance, in the T1-weighted data of the brain GCV is the more appropriate technique in view of the occurrence of overregularized pixels with LCC; on the other hand, LCC is a more desirable option in CT data since only a minimal in-slice smoothing window is required to remove underregularized pixels. However, in view of the difficulty to eliminate underregularized pixels with GCV in certain classes of data (in particular the renal data), we chose LCC as a default method in current implementations.

From a quantitative perspective, the patient data as well as the simulations suggest that the distinction between LCC and GCV is relevant mainly in data with large (random or systematic) measurement error: at higher values of SNR in data where no obvious systematic error is present, both methods appear in good agreement. In this sense, one could hypothesize that a comparison between LCC and GCV results provides an objective criterion to decide whether the data quality is sufficient for accurate quantification. A definite answer to this question can only be reached by performing simulations which include, apart from random noise, a representative selection of structured error in the data.

6. Conclusion

We conclude that the reported problems with image quality can be removed by appropriate optimization of either the L-curve criterion or generalized cross validation. In all examples this could be achieved with LCC without significant perturbation of the values in pixels where the regularization parameter was originally selected accurately. GCV could not be optimized for the renal data, and only at the cost of some image resolution in the CT data. Using the implementations given, calculation times are sufficiently short for routine application in the clinic.

References

- Calamante F, Gadian D G and Connelly A 2000 Delay and dispersion effects in dynamic susceptibility contrast MRI: simulations using singular value decomposition *Magn. Reson. Med.* **44** 466–73
- Carpenter T, Armitage P, Bastin M and Wardlaw J 2006 DSC perfusion MRI-quantification and reduction of systematic errors arising in areas of reduced cerebral blood flow *Magn. Reson. Med.* **55** 1342–9
- Cenic A, Nabavi D G, Craen R A, Gelb A W and Lee T-Y 2000 A CT method to measure hemodynamics in brain tumors: validation and application of cerebral blood flow maps *Am. J. Neuroradiol.* **21** 462–70
- Corbard T, Berthomieu G, Provost J and Morel P 1998 Inferring the equatorial solar tachocline from frequency splittings *Astron. Astrophys.* **330** 1149–59
- Duhamel G, Schlaug G and Alsop C 2006 Measurement of arterial input functions for dynamic susceptibility contrast magnetic resonance imaging using echoplanar images: comparison of physical simulations with *in vivo* results *Magn. Reson. Med.* **55** 514–23
- Dujardin M, Sourbron S, Luypaert R, Verbeelen D and Stadnik T 2005 Quantification of renal perfusion and function on a voxel-by-voxel basis: a feasibility study *Magn. Reson. Med.* **45** 841–9
- Farquharson C G and Oldenburg D W 2004 A comparison of automatic techniques for estimating the regularization parameter in non-linear inverse problems *Geophys. J. Int.* **156** 411–25
- Hansen P C 1992 Analysis of discrete ill-posed problems by means of the L-curve *SIAM Rev.* **34** 561–80
- Hansen P C 1998 *Rank-Deficient and Discrete Ill-Posed Problems* (Philadelphia, PA: SIAM)
- Hoeffner E G, Case I, Jain R, Gujar S K, Shah G V, Deveikis J P, Carlos R C, Thompson B G, Harrigan M R and Mukherji S K 2004 Cerebral perfusion CT: technique and clinical applications *Radiology* **231** 632–44

- Jacquez J A 1985 *Compartmental Analysis in Biology and Medicine* 2nd edn (Ann Arbor, MI: University of Michigan Press)
- Jerosch-Herold M, Swingen C and Seethamraju R T 2002 Myocardial blood flow quantification with MRI by model-independent deconvolution *Med. Phys.* **29** 886–97
- Koh T S and Hou Z 2003 A numerical method for estimating blood flow by dynamic functional imaging *Med. Eng. Phys.* **24** 151–8
- Koh T S, Wu X Y, Cheong L H and Lim C C T 2004 Assessment of perfusion by dynamic contrast-enhanced imaging using a deconvolution approach based on regression and singular value decomposition *IEEE Trans. Med. Imaging* **23** 1532–42
- Lassen N A and Perl W P 1979 *Tracer Kinetic Methods in Medical Physiology* (New York: Raven Press)
- Liu H L, Pu Y, Liu Y, Nickerson L, Andrews T, Fox P T and Gao J H 1999 Cerebral blood flow measurement by dynamic contrast MRI using singular value decomposition with an adaptive threshold *Magn. Reson. Med.* **42** 167–72
- Makkat S, Sourbron S, Dujardin M, Van Schuerbeek P, Luypaert R and Stadnik T 2005 Deconvolution-based contrast enhanced MR imaging of breast tumors for perfusion quantification: a feasibility study *Proc. Int. Soc. Mag. Reson. Med. (Miami)* p 743
- Murase K, Shinohara M and Yamazaki Y 2001 Accuracy of deconvolution analysis based on singular value decomposition for quantification of cerebral blood flow using dynamic susceptibility contrast-enhanced magnetic resonance imaging *Phys. Med. Biol.* **46** 3147–59
- Østergaard L, Weisskoff R M, Chesler D A, Gyldensted C and Rosen B R 1996a High resolution measurement of cerebral blood flow using intravascular tracer bolus passages: Part I. Mathematical approach and statistical analysis *Magn. Reson. Med.* **36** 715–25
- Østergaard L, Sorensen A G, Kwong K K, Weisskoff R M, Gyldensted C and Rosen B R 1996b High resolution measurement of cerebral blood flow using intravascular tracer bolus passages: Part II. Experimental comparison and preliminary results *Magn. Reson. Med.* **36** 726–36
- Smith M R, Lu H, Trochet S and Frayne R 2004 Removing the effect of SVD algorithmic artefacts present in quantitative MR perfusion studies *Magn. Reson. Med.* **51** 631–4
- Sorensen A G and Reimer P 2000 *Cerebral MR Perfusion Imaging* (Stuttgart: Georg Thieme Verlag)
- Sourbron S 2005 Perfusion quantification with bolus-tracking MRI *PhD Thesis* Vrije Universiteit Brussel
- Sourbron S, Luypaert R, Van Schuerbeek P, Dujardin M, Stadnik T and Osteaux M 2004a Deconvolution of dynamic contrast-enhanced MRI data by linear inversion: choice of the regularization parameter *Magn. Reson. Med.* **52** 209–13
- Sourbron S, Luypaert R, Van Schuerbeek P, Dujardin M and Stadnik T 2004b Choice of the regularization parameter for perfusion quantification with MRI *Phys. Med. Biol.* **49** 3307–24
- Sourbron S, Dujardin M, Luypaert R, Van Schuerbeek P, Makkat S, De Ridder F, Chaskis C and Stadnik T 2005 Characterization of brain tumors with bolus tracking data: T1 weighted MRI versus CT *Proc. Int. Soc. Magn. Reson. Med. (Miami)* p 2097
- Wahba G 1977 Practical approximate solutions to linear operator equations when the data are noisy *SIAM J. Numer. Anal.* **14** 651–67